

1 A dynamic lithosphere-asthenosphere boundary near the
2 equatorial Mid-Atlantic Ridge

3 Catherine A. Rychert^{1*}, Saikiran Tharimena², Nicholas Harmon¹, Shunguo Wang³, Steven
4 Constable⁴, J. Michael Kendall⁵, Petros Bogiatzis¹, Matthew R. Agius⁶ and David
5 Schlaphorst⁷

6 ¹*Ocean and Earth Science, National Oceanography Centre Southampton, University of
7 Southampton Waterfront Campus, UK*

8 ²*Faculty of Earth Sciences, Geography and Astronomy, University of Vienna, Austria*

9 ³*Norwegian University of Science and Technology, Norway*

10 ⁴*Scripps Institution of Oceanography, University of California, San Diego, San Diego, CA, USA*

11 ⁵*Earth Sciences, University of Oxford, UK*

12 ⁶*Department of Sciences, University of Roma Tre, Rome, Italy*

13 ⁷*Instituto Dom Luiz (IDL), Faculdade de Ciências, Universidade de Lisboa, Campo Grande,
14 1749-016, Lisboa, Portugal*

15

16

17

18 **ABSTRACT**

19 **In plate tectonic theory a weak asthenosphere is required to facilitate the motions of the**
20 **rigid plates. Partial melt could weaken the mantle, in turn impacting convection, but to**
21 **date the existence of persistent melt has remained controversial. A wide range of scenarios**
22 **have been reported in terms of the location, amount and pathways of melt. Here we use**

23 data collected by 39 ocean bottom seismometers deployed near the equatorial Mid-Atlantic
24 Ridge on 0 to 80 Myr old seafloor. We calculate S-to-P (Sp) receiver functions and perform
25 waveform modeling. We jointly interpret with shear-wave velocity tomography from
26 surface waves and magnetotelluric (MT) imaging to take advantage of a range of
27 resolutions and sensitivities and illuminate the structure of the oceanic lithosphere and the
28 underlying asthenosphere. We image a tectonic plate thickness that increases with age in
29 one location but undulates in another location. We infer thin and slightly thicker melt
30 channels and punctuated regions of ascending partial melt several hundred kilometers off
31 the ridge axis. This suggests melt persists over geologic timescales, although its character is
32 dynamic, with implications for the lithosphere-asthenosphere boundary (LAB) and the
33 driving forces of the plates. Ascending melt intermittently feeds melt channels at the base
34 of the plate. The associated melt-enhanced buoyancy increases the influence of ridge-push
35 in driving plate motions, whereas the channelized melt reduces the resistance of the plates
36 to motion. Therefore, melt dynamics may play a larger role in controlling plate tectonics
37 than previously thought.

38 **Keywords:** oceanic lithosphere-asthenosphere boundary, seismology, Mid-Atlantic Ridge,
39 plate tectonics, receiver functions, melt dynamics

40 1. INTRODUCTION

41 *1.1 MELT AND THE NATURE OF THE LITHOSPHERE ASTHENOSPHERE* 42 *BOUNDARY*

43 A large number of observations including imaging of sharp seismic discontinuities,
44 strong electrical conductivity anomalies, slow seismic velocities and plate thicknesses that do not
45 monotonically increase with age are inconsistent with a purely thermal definition for the tectonic
46 plate (Forsyth et al., 1998; Kawakatsu et al., 2009; Key et al., 2013; Naif et al., 2013; Rychert et

47 al., 2018b; Rychert and Shearer, 2009; Thybo, 2006). Several subsolidus mechanisms have been
48 invoked to explain individual observations that do not conform to the classical thermal model of
49 a plate (Beghein et al., 2014; Burgos et al., 2014; Cline et al., 2018; Karato et al., 2015;
50 Yamauchi and Takei, 2016); although, each of these fails to universally explain all aspects of the
51 aforementioned observations (Rychert and Harmon, 2018; Rychert et al., 2018b). Alternatively,
52 partial melt may exist in the asthenosphere (Kawakatsu et al., 2009). Melt is expected to decrease
53 the viscosity of the mantle (Hirth and Kohlstedt, 1995; Jackson et al., 2006), which could in turn
54 influence mantle dynamics including the coupling of the plate to the deeper mantle and the
55 thickness of the plate with potential implications for the driving forces of plate tectonics.

56 Despite its importance, constraining the amount, locations, and pathways of melt has
57 proved challenging, especially near oceanic spreading centers where new plates are formed.
58 Reports of melt are varied and come from different imaging techniques and locations. Shear
59 velocities inferred from surface waves suggest melt exists over a broad area beneath the ridge,
60 out to 400 km off-axis (Forsyth et al., 1998), whereas MT data suggests a narrow triangle, out to
61 20 km off-axis (Key et al., 2013). Seismic imaging from receiver functions, SS precursors, and
62 approaches that include multiple S bounces implies sharp discontinuities that require melt
63 beneath the plate over large swaths of the mantle (Gaherty et al., 1996; Kawakatsu et al., 2009;
64 Rychert et al., 2018b; Tan and Helmberger, 2007), with a structure in which melt percentage
65 gradually decrease with depth over tens of kilometers or more (Rychert and Harmon, 2018). Two
66 seismic reflection surveys and one MT study imaged thin melt channels (Mehouachi and Singh,
67 2018; Naif et al., 2013; Stern et al., 2015) possibly caused by ponding along a permeability
68 boundary (Sparks and Parmentier, 1991), although this has not been imaged everywhere (Key et

69 al., 2013). Questions remain as to the exact geometry, location, volume, and pervasiveness of
70 melt in the mantle and its relationship to the LAB.

71 Spreading rate is thought to be a key factor in determining the style of mantle flow,
72 associated melting, and plate characteristics (Morgan et al., 1987; Parmentier and Morgan,
73 1990). However, to date much imaging of the mantle has been focused on the Pacific. For
74 example, the fast-spreading East Pacific Rise (EPR) has been shown to be dominated by 2-D
75 passive upwelling (Forsyth et al., 1998; Key et al., 2013), although an asymmetric sub-ridge
76 anomaly (Forsyth et al., 1998) may also indicate additional influences such as across axis flow
77 owing to lateral pressure or thermal gradients (Conder et al., 2002; Toomey et al., 2002), local
78 melt buoyancy (Katz, 2010), or small scale convection (Harmon et al., 2011). Passive upwelling
79 has also been inferred near the intermediate spreading Juan De Fuca and Gorda Ridges (Bell et
80 al., 2016) but again with asymmetry suggesting additional influences, potentially the nearby
81 Cobb hotspot. End member slow spreading at the Mid-Atlantic Ridge has not yet been
82 investigated at a large scale and with a range of methods.

83 We installed 39 broadband ocean bottom seismometers and 39 ocean bottom
84 MT instruments on and around the equatorial Mid-Atlantic Ridge, in the region of the Chain
85 Fracture Zone from March 2016 to March 2017 (Fig. 1) (Harmon et al., 2020; Harmon et al.,
86 2018; Wang et al., 2020). The deployment was part of the PI-LAB (Passive Imaging of the LAB)
87 experiment, the EURO-LAB (Experiment to Unearth the Rheological Oceanic LAB), and the
88 CA-LAB (Central Atlantic imaging of the LAB) experiment, to study a slow spreading ocean
89 plate from its formation to an age of 80 Myr with a range of sensitivities and resolutions. Here
90 we present new Sp receiver function imaging and waveform modeling of discontinuity structure
91 (Rychert et al., 2018a). We jointly interpret with shear-wave velocity tomography from surface

92 waves using teleseismic earthquakes and ambient noise (Harmon et al., 2020) and 2-D MT
93 imaging (Wang et al., 2020) for a conceptual model of the dynamics of the region.

94 **1.2 A BRIEF SUMMARY OF PREVIOUS MT AND SURFACE WAVE IMAGING**
95 **RESULTS**

96 Previous imaging in the PI-LAB study region revealed a thickening fast lid, several
97 punctuated asthenospheric slow velocity zones and low resistivity anomalies, and also one fast
98 and resistive asthenospheric anomaly (Harmon et al., 2020; Wang et al., 2020). Several MT
99 anomalies are in good agreement with those inferred from surface waves. For instance, using the
100 nomenclature of Harmon et al., (2020) and Wang et al., (2020), which we will continue to use
101 here, high conductivity and slow seismic velocity at anomalies B, C, and F and high resistivity
102 and fast seismic velocity at anomaly D as labelled for instance in Figure 1. The MT anomaly is
103 shallower than the shear-wave anomaly inferred from surface waves at A, further west near B,
104 thinner and broader than the shear-wave anomaly inferred from surface waves near F, and further
105 west (shallower and deeper) near E. Seismic velocities need not match MT anomalies given that
106 they have different sensitivities to the properties of the Earth. For instance, seismic waves are
107 more sensitive to grain size and also seismic anisotropy caused by mineral alignment than MT.
108 However, the locations of the anomalies are not discrepant given the resolutions of the
109 methodologies (e.g., ~100 km lateral resolution, 10s km depth resolution for surface waves).
110 General agreement between the models suggests temperature and melt, the factors that do impact
111 both methodologies, are dominant (Harmon et al., 2020; Wang et al., 2020). Anomalies A, B and
112 E are likely associated with sub-ridge upwelling and decompression melting. However,
113 anomalies C and F are too far from the axis, to be ridge related, while anomaly D appears to be a
114 lithospheric drip, and taken together suggest small scale convection. Receiver function imaging
115 provides a means of testing the sharpness of the seismic LAB and provides further constraints on

116 the character of melt at the base of the lithosphere that cannot be provided by shear-wave
117 velocity based on surface waves alone.

118 2. Methods

119 2.1 *RECEIVER FUNCTION IMAGING*

120 We used seismic data from teleseismic events located at epicentral distances 55° to 80° .

121 We considered all events with magnitude > 5.5 . The data were rotated into P- and S-wave
122 components using a transformation matrix for ocean bottom seismometers (Rychert et al.,
123 2018a). For rotation of data, we used previously determined sediment velocities based on the P-
124 to-S delay times from the sediment crust conversion and velocity-thickness relationships from
125 previous work (Agius et al., 2018; Saikia et al., 2020). For stations where no P-to-S constraint or
126 admittance constraint existed we used the linear interpolation between stations as reported in the
127 P-to-S paper (Agius et al., 2018). We assumed a density of 2900 kg/m^3 . The waveforms were
128 bandpass filtered from 0.02 to 0.23 Hz. We tested a range of other bands. We found that the
129 interpreted features persisted regardless of the exact band used. However, this band was most
130 desirable in terms of the simplicity of the deconvolved waveforms. This band is also similar to
131 that used in previous ocean bottom receiver function studies (Rychert et al., 2018a).

132 We visually inspected both the P- and S-wave components near the theoretical S-wave
133 arrival on 3,319 waveforms. We selected waveforms with visible arrivals on the S-wave
134 component, and with an S-wave amplitude larger than amplitudes before or after its arrival.
135 Some energy was predicted on the P-wave component owing to conversions from the base of a
136 sediment layer. We discarded waveforms where the apparent S-wave arrival was greater than 10
137 s off the theoretical arrival. We manually selected a window around the visible S-wave arrivals
138 to use as the source waveform in deconvolution. After handpicking the data, we were left with
139 801 waveforms.

140 The data were deconvolved using an extended time multitaper method (Helffrich, 2006;
141 Rychert et al., 2012) using a 50 s window, $NW = 3$, and 4 tapers (Shibutani et al., 2008). The
142 deconvolved waveforms were inverted so that positive phases correspond to velocity increases
143 with depth, consistent with polarity typical for P-to-S receiver functions. The waveforms were
144 then migrated and stacked on a $0.5^\circ \times 0.5^\circ$ grid, with a depth spacing of 1 km. For migration, we
145 used a modified version of PREM to include estimated sediment properties (Agius et al., 2018;
146 Saikia et al., 2020) and an oceanic crust of 7 km. In the crust we assumed a V_P/V_S ratio that
147 varied with distance from the ridge from 2.0 to 1.77, to simulate the effect of near-ridge melt. In
148 the mantle we assumed V_P/V_S ratio = 1.77. For stations with no sediment thickness information,
149 we used the linear interpolation between stations, calculating V_S and V_P based on relationships
150 from previous work as explained in the P-to-S study (Agius et al., 2018). We corrected for
151 station elevations in the migration process and only used bins with more than three waveforms in
152 the stack (Fig. 2). We smoothed the bins over the Fresnel zone of the waves with a minimum
153 Fresnel zone cutoff of 50 km.

154 We tested the effect of a range of migration models. We tested using both P- and S-wave
155 velocities from PREM (Dziewonski and Anderson, 1981), modified to include the sediment layer
156 along with a 7 km crust. We also tested a constant crustal V_P/V_S ratio with distance from the
157 ridge, the effect of using constant vs. varying sediment thickness, and also using a full 3D shear
158 velocity model inferred from inversion of surface waves from this study and calculating the P-
159 wave velocity, assuming a range of constant V_P/V_S ratios (1.77 – 2.0) and also varying them with
160 distance. We also tested using PREM (Dziewonski and Anderson, 1981) and a range of V_P/V_S in
161 the range of 1.77 to 2.0, i.e. an increase in P-wave velocity of 1.5 % to 14.5 % compared to
162 PREM P-wave velocities.

163 The features interpreted here were present in all of these tests with variable degrees of
164 clarity, suggesting that they are the robust features. In addition, there was no significant change
165 in the discontinuity depths and/or the age-depth trend of the LAB phase. A 5% faster model
166 causes discontinuities near 30 – 40 km depth to migrate 1 km shallower and vice-versa if slower
167 velocities are assumed, while still maintaining the age-depth relationship of the LAB phase.
168 However, if larger V_P/V_S is used at the ridge and lower V_P/V_S away from the ridge, the
169 discontinuities beneath the ridge migrate shallower by $\sim 2 - 3$ km, enhancing the age-depth trend.
170 Although phases at greater delay times/deeper depths have the potential to be more influenced by
171 migration model choices, V_P/V_S variations beneath thicker, melt-free lithosphere are predicted to
172 be less, making the overall expected effect moderate. We tested the potential impact of an
173 inaccurate V_P/V_S assumption in the migration model by changing mantle V_P by 5%, which
174 resulted in 5 km shifts in phases around 80 km deep. Therefore, we report error in the depth of
175 the discontinuities as ± 5 km, encompassing modest migration model variations beneath older
176 lithosphere and strong variations beneath younger lithosphere. We interpret phases that are
177 significantly different from zero according to error bounds calculated for 95 % confidence (Fig.
178 3). We show the depth and locations of where we detected the LAB phase above the threshold of
179 formal error in Fig. 2.

180 **2.2 RECEIVER FUNCTION WAVEFORM MODELING**

181 We modeled the receiver function waveforms at anomalies A, C, D, E, and F with
182 synthetic seismograms, processing them in the identical way as the data. We modeled the
183 receiver functions in two ways to illustrate the range of potential models that fit the data. We did
184 not model anomaly B given that there is not a significant receiver function and the locations of
185 the resistivity and shear-wave anomalies from surface waves are not spatially coincident, likely
186 owing to variable resolutions of heterogeneous structures. Disambiguating complexity at

187 anomaly B is beyond the scope of this study. We first forward modeled the data assuming a
188 minimum parameterization, that included one Moho layer, one lithospheric layer and one
189 asthenospheric layer. We allowed the layer thicknesses and shear velocities to vary. We also
190 performed a discretized layer inversion using 10 km thick layers. We permitted shear velocity
191 and V_p/V_s in the layers to vary between 3.8 - 4.8 km/s and 1.7 - 2.0, respectively, with the
192 remaining assumptions the same as for the forward approach. We also tested a range of fixed
193 V_p/V_s , although it did not impact our overall result, i.e., beyond our error bars. The minimum
194 parameterization is appealing in that it provides the simplest solution. The discretized inversion
195 illustrates the endmember case for smoother gradients. The approach could be considered an
196 overparameterization. However, the results of the inversions were primarily simple gradient
197 structures, which could instead be described by sharpness and magnitude rather than the
198 velocities of each individual step without created unresolved degrees of freedom. Therefore, we
199 use this approach to illustrate how smooth the gradients could be while still matching the data.

200 **3. RESULTS**

201 **3.1 RECEIVER FUNCTION IMAGING RESULTS**

202 Sp receiver functions image a velocity increase with depth at 4 – 8 km below the seafloor
203 across the region associated with the Moho (Figs. 4). At greater depths Sp images a negative
204 phase. Synthetic waveform modeling suggests it is consistent with a sharp velocity decrease of 6
205 – 15 % over < 30 km depth (see section 3.2). The depth of the velocity contrast increases
206 monotonically with age in the western side of transect II in the south from 30 to 80 ± 5 km depth
207 below sea level (Figs. 4, S1, S2). In the eastern side of transect II the negative phase is patchy. In
208 transect I in the north the phase has more complex topography and is characterized by larger
209 error and a patchy character (Figs. 2 - 4). The transects and therefore the interpretations are
210 located in regions where the hit count is high, and therefore LAB detection vs. non-detection

211 must be either real or an artefact of S-to-P resolution (Fig. 2), which we address in subsequent
212 sections. We do not interpret features that are not significantly different from zero according to
213 formal error and therefore, by definition they cannot be noise. In addition, the interpreted
214 features are clearly present in the highest quality receiver functions and do not arise from noise
215 (Fig. S1).

216 **3.2 RECEIVER FUNCTION MODELING RESULTS**

217 We find good fits to the receiver function waveforms using the minimum parameterization
218 approach (Fig. 5). We find strong, sharp velocity drops at the LAB at anomalies A (8 % at 36
219 km), C (11 % at 43 km), E (13 % at 34 km) and F (15 % at 39 km). No negative LAB
220 discontinuity is required to match the receiver functions at anomaly D. We do not attempt to fit
221 additional phases by adding discontinuities, given that we limit the number of parameters, in
222 particular the second negative peak at anomaly A. The additional peak could be real,
223 representing continued drop in velocity or they could represent smearing of slightly different
224 LAB depth in nearby bins, given strong nearby lateral variability (Fig. 4).

225 In the discretized approach, we find that we also fit the receiver function waveforms well.
226 In this parameterization the LAB phase is explained by smoother velocity depth profiles that still
227 include large velocity drops from the highest to the lowest velocity: A (12 % from 30 - 50 km
228 depth), C (6 % at 40 km depth), E (11 % from 30 - 40 km depth), and F (13 % from 20 - 50 km
229 depth). At anomaly D a broad and moderate velocity drop (7 % from 20 to 50 km depth) can also
230 be included, while still fitting the data. At anomaly A the discretized inversion prefers a broad
231 velocity gradient to produce a better match the second negative pulse, within the error bounds.
232 However, we did not force a fit to within error given that the deeper pulse could be caused by
233 lateral smearing of nearby topography on the gradient.

234 **4. DISCUSSION**

235 **4.1 COMPARISON OF RECEIVER FUNCTIONS TO RESISTIVITY AND SHEAR-**
236 **WAVE VELOCITIES FROM SURFACE WAVES**

237 There is good agreement with the depth of the discontinuity beneath the western half of
238 transect II and most other reported discontinuity depths from scattered waves and transect studies
239 beneath the oceans unaffected by hotspot volcanism globally (Fig. 6). There is also agreement
240 with the depths of the lowest velocities from surface waves from a global model across the
241 Pacific (French et al., 2013). However, there are also regions that exhibit significant deviations,
242 for instance beneath other areas of our study region and also beneath ocean islands or regions
243 affected beneath hotspots. This suggests that while on average temperature plays a large role in
244 dictating the thickness of the lithosphere, there are also important deviations (Rychert et al.,
245 2020). Here we will explore these further.

246 There is good agreement between the presence of a significant negative receiver function
247 phase and locations of underlying slow shear-wave velocity anomalies inferred from inversion of
248 surface waves (< 4.2 km/s) at 50 – 100 km depth (Fig. 4, 5, 7 anomalies A C, E, and F) and also
249 locations where moderate MT conductivities extend to greater depths, i.e., greater than a thin 10
250 km channel (Fig. 5 e.g., anomaly B, C, F, and just west of E). The negative receiver function
251 phase is absent or insignificant from zero where the high velocity, high resistivity drip occurs
252 (Fig. 5, 7 anomaly D), where the conductivity anomaly is a thin channel (Fig. 7 either side of
253 anomaly F) and where the depth of the negative receiver function phase undulates, based on the
254 punctuated shear-wave velocity anomalies from surface waves and MT anomalies (sections of
255 transect I).

256 The relationship of the significant negative receiver function phases to the strong shear-
257 wave anomalies from surface waves and moderate MT anomalies over broader depths is likely
258 explained by differences in resolution. MT can resolve thin channels on the order of 10 km

259 (Parker and Whaler, 1981), whereas Sp suffers from destructive interference. For instance, the
260 amplitude of conversions from the top of a 10 or a 5 km thick channel would be reduced to ~70
261 % and ~30 % of the original values, respectively, for the filtering used here (Rychert and
262 Harmon, 2018), beneath the detectability threshold from our receiver function error analysis.
263 Therefore, the locations where receiver functions clearly image a singular negative velocity
264 discontinuity likely represent locations where low velocity zones exist over > 10 km depth,
265 gradually increasing in velocity with depth.

266 The lack of significant negative receiver function phases adjacent to punctuated shear-
267 wave velocity anomalies from surface waves and MT imaging is likely also explained by
268 resolution. The shear-wave tomography based on local Rayleigh waves images near vertical
269 edges to anomaly structures at 30 to 55 km beneath the ridge in transect I (Saikia et al., 2021).
270 Sp cannot easily resolve dipping or undulating topography (Lekic and Fischer, 2017) (Fig. 7
271 transect I particularly near anomaly B).

272 In light of the different resolutions of the three approaches, the patchy receiver function
273 imaging of negative discontinuities is expected. The association of the negative phase with the
274 base of the seismically fast lithosphere from surface waves and the resistive lithosphere from MT
275 imaging suggests it marks the LAB.

276 Overall, Sp LAB phases together with MT imaging and surface waves illuminate the
277 structure of the lithosphere and the asthenosphere. In the western side of transect II, the plate
278 thickens relatively monotonically with age (Fig. 4, 7, S2) and is characterized by a single
279 velocity drop rather than a thin channel (drop followed by a deeper velocity increase) (see
280 section 4.2 and Fig. 2, 7). In the eastern section of transect II the lithosphere is underlain by a
281 channel that is thinner (~10 km) close to the ridge and extending to 10 - 15 Myr. Near anomaly F

282 the channel is thicker (> 10 km), flatter, and gradually tapers with depth. In transect I the
283 seismically fast and resistive plate undulates in thickness with age, and there is a single velocity
284 drop in some regions, such as anomaly C. No channel is apparent.

285 **4.2 1-D MODEL COMPARISONS AND RECEIVER FUNCTION MODELING**

286 We compare the receiver functions to the surface wave and MT models in the locations
287 of the discrete major asthenospheric anomalies. The 1-D profiles through anomalies A, C, E and
288 F all show LAB receiver function peaks that are significant from zero. The depths of the peaks
289 all fall within the gradual drops in shear-wave velocity with depth at the base of the plate (Fig. 4
290 - 6). Shear-wave velocities in the slow anomalies also reach as slow as 4.2 km/s or slower in the
291 surface wave model. In contrast, at anomaly D no strong sharp phase is required by the receiver
292 function and shear-wave velocities are fast ($V_s > 4.4$ km/s over the upper 150 km of the mantle)
293 in the location of a hypothesized lithospheric drip. Anomaly A is slightly shallower in the MT
294 imaging than the seismic, potentially owing to resolution. Anomaly B and C are muted in the
295 receiver functions, which is likely explained by lateral variability in the depth of the phase, as
296 evidenced by undulating contours from MT and surface waves. The overall agreement among the
297 independent seismic methods for anomalies A, C, D, E and F gives us confidence in these
298 features.

299 The exact shapes of the velocity profiles of the receiver function models and the shear-
300 wave velocities inferred from surface waves are different at least for some anomalies and some
301 parameterizations. While the best-fitting receiver function models fall outside the formal error
302 bars on the shear-wave velocities inferred from surface waves, the two are not necessarily
303 discrepant. The sensitivity kernels of the shear-wave velocities from surface waves (Harmon et
304 al., 2020) mean that the inferred shear-wave velocities are smoothed over a depth range and the
305 error bars represent uncertainty in the average over that depth range rather than uncertainty in the

306 velocity at any single depth. Therefore, the shear velocity from surface wave modeling cannot
307 be simply compared with the receiver function result at any single depth.

308 Overall, the modeling results provide a range of potential models that could fit the data.
309 Anomalies A, C, E, and F all require strong, sharp velocity gradients: A (8 - 12 % over < 20 km),
310 C (6 - 11 % over 0 km), E (11 - 13 % over < 10 km) and F (13 - 15 % over < 30 km). None can
311 be explained by a purely thermal model such as half-space cooling or the plate cooling model
312 which are characterized by broader velocity gradients (over > 40 km depth) beneath 0 - 30 Myr
313 old lithosphere (Tharimena et al., 2017), none of which are predicted to produce a converted
314 receiver function strong enough for interpretation (Rychert and Harmon, 2018). Of course, there
315 are error bars on the data which might allow for smaller velocity drops, particularly for
316 anomalies C and F. However, this would not be consistent with the shear-wave velocity model
317 from surface waves, which overall shows very good agreement with the total drop from the
318 receiver functions and requires absolute velocities < 4.2 km/s in the asthenosphere. This suggests
319 that muted receiver function amplitudes and error bars at C and F are more likely a product of
320 lateral variability of depth of the discontinuity, and sharp discontinuities inconsistent with a
321 thermal model are required at anomalies A, C, E, and F.

322 **4.3 COMPARISON OF LITHOSPHERE-ASTHENOSPHERE STRUCTURE**

323 The sub-ridge lithosphere from receiver functions, surfaces waves, and MT imaging is
324 thicker (20 – 25 km) than the non-existent plate beneath the fast spreading EPR (Harmon et al.,
325 2009; Key et al., 2013), and equal to or thicker than the 20 km thick plate beneath the
326 intermediate spreading ridges in Cascadia (Rychert et al., 2018a). This trend of thicker sub-ridge
327 lithosphere for slower spreading rates is predicted for lateral conductive cooling (Morgan et al.,
328 1987).

329 The high conductivity channel from MT is similar to some previous channels imaged
330 north of our study area (Mehouachi and Singh, 2018) and beneath the Cocos (Naif et al., 2013)
331 and Pacific Plates (Stern et al., 2015). However, it is dissimilar with the lack of a channel
332 imaged, for instance, in the remainder of our study area and also near the EPR and Mohns Ridge
333 (Baba et al., 2006; Forsyth et al., 1998; Johansen et al., 2019; Key et al., 2013).

334 The apparent extreme thickening, or drip-like feature at 30 Myr (Figs. 4 - 6, anomaly D)
335 and also the punctuated anomalies off-axis (e.g., C and F) differ from the smooth, monotonic
336 increases in plate thickness in the western side of transect II and as observed in the MELT
337 experiment (Harmon et al., 2009) and Cascadia (Rychert et al., 2018a). Punctuated anomalies
338 that are distant from the ridge axis are also different from the previously imaged singular,
339 focused sub-ridge anomalies of other studies (Baba et al., 2006; Forsyth et al., 1998; Johansen et
340 al., 2019; Key et al., 2013), although our study includes a variety of sensitivities and extends to
341 ages 8 – 25 times older than these studies.

342 **4.4 A DYNAMIC LITHOSPHERE-ASTHENOSPHERE SYSTEM**

343 Several aspects of the observations are not consistent with a model that includes purely
344 conductive cooling. The receiver function phases require sharp velocity gradients (6 – 15 % over
345 < 30 km). Subtle negative receiver function phases can be produced for thermal models (Fischer
346 et al., 2020; Rychert and Harmon, 2018), although these are smaller than the requirements of our
347 observations. Thermal gradients over the broadest 20 – 30 km depth ranges from our waveform
348 modelling can only explain about a 4 % drop (Jackson and Faul, 2010). Similarly, the
349 magnitudes of the high conductivity anomalies (< 1 Ω m) cannot be explained by and slow
350 seismic velocities (V_s < 4.2 km/s), channels structures, and punctuated off-axis anomalies are not
351 explained by thermal models (Harmon et al., 2020; Wang et al., 2020).

352 Several sub-solidus mechanisms have been proposed to explain observations that are
353 discrepant from thermal models. Seismic anisotropy from the alignment of olivine does not
354 affect MT data, and therefore can be excluded in all locations where the methods agree. Also,
355 Rayleigh wave anisotropy using local events is generally small $< 3\%$ throughout the study area
356 (Saikia et al., 2021), and associated impacts on seismic imaging would be very low (Rychert and
357 Harmon, 2018). Near solidus temperatures can cause very low seismic velocities (Yamauchi and
358 Takei, 2016), although this would not explain the MT imaging, and it is also likely that the
359 mantle near a mid-ocean ridge system will be above the solidus temperature. Mantle oxidation
360 may affect seismic waves (Cline et al., 2018), but this is expected to be low at mid-ocean ridges
361 and therefore not likely a factor. In the elastically accommodated grain boundary sliding model
362 an increase in the sharpness of the velocity gradient with age is predicted, which would cause
363 larger amplitudes and/or more impulsive receiver function phases at older ages (Karato et al.,
364 2015), but this is not observed. In addition, this model would not likely affect MT data. Finally,
365 recent laboratory experiments suggest that water does not affect observed seismic wave
366 velocities (Cline et al., 2018), and the amount of hydration required to explain the magnitude of
367 the conductivity anomalies would necessarily mean that the mantle is partially melted (Key et al.,
368 2013).

369 Alternatively, partial melt could explain the sharp decreases in seismic velocity with
370 depth, the slowest seismic velocity anomalies, the lowest resistivities, and the channelized and
371 punctuated anomaly structures. Slow shear-wave velocity anomalies inferred from surface waves
372 were reported to be 1 – 3 % (Harmon et al., 2020) in comparison to experimental predictions for
373 peridotite at asthenosphere conditions (Jackson and Faul, 2010). Comparison to receiver function
374 profiles suggests general agreement in terms of the slowest asthenosphere velocities, but a

375 sharper transition from the fast lithosphere to the slower asthenosphere, and therefore a locally
376 more pronounced anomaly than predicted by experimental predictions for thermal models or
377 resolvable by surface waves (Fig. 5). Therefore, we proceed considering the new tighter
378 constraints on the strong sharp drop from receiver functions. The receiver functions require a
379 velocity drop of 6 – 15%. A thermal gradient at the base of the plate could explain up to a 4 %
380 velocity drop for the broader, 20 – 30 km, gradients of the discretized model corresponding to
381 the larger velocity drops (Jackson and Faul, 2010), i.e., not the 6 % drop over 0 km at anomaly 6.
382 Therefore, after accounting for the maximum effect of temperature we are left with a 6 – 11 %
383 velocity drop. Assuming a 2.7% velocity reduction per 1% melt fraction for melt distributed in
384 tubules (Hammond & Humphreys, 2000) or 2.0% velocity reduction per 1 % melt fraction
385 assuming equilibrium melt geometries (e.g., Clark & Leshner, 2017), suggests melt fractions, 2.2
386 – 5.5 %. Alternatively, if melt exists in films it could result in an 7.9 % drop in velocity per 1%
387 percent partial melt, suggesting melt fractions of 0.8 – 1.4 %. These estimates from receiver
388 functions are in good agreement with the predicted melt fractions at the lower end of MT
389 modeling which require 1 – 7 % melt (Wang et al., 2020). Considered together the seismic and
390 MT results can be explained by 1 – 5.5 % melt.

391 Our observations suggest two different configurations for melt, both channelized at the
392 base of the plate and distributed in distinct broad regions with length scales on the order of 100
393 km or more (Fig. 8). The melt channels are characterized by variability in the sharpness in the
394 gradients in melt volume at their base. Seismic and MT imaging together suggests a thicker
395 channel with gradual drop off in melt percentage with depth in the western side of transect II, a
396 thinner, sharper channel (10 km or less) in most of the eastern side of transect II, a thicker

397 channel with gradual drop off with depth in the vicinity of anomaly F, and the lack of a channel
398 in transect I (see section 4.2).

399 The existence of melt with variable character is supported by recent geodynamic
400 modeling with non-Newtonian viscosity and two-phase flow that produces ‘porosity waves’,
401 ephemeral melt-rich pockets that rise from depth and become thicker and more closely spaced as
402 they approach and pond beneath permeability boundaries at shallow depths (Sim et al., 2020).
403 Our punctuated anomalies particularly in transect I (e.g., anomaly C) are consistent with rising
404 melt. Whereas melt beneath the plate over a broad depth range (near anomaly E) and in a thin
405 channel (west of anomaly F) in transect II could represent melt ponded beneath the plate. The
406 lack of an imaged channel in transect I could imply the ponded melt in the region has left the
407 system and has yet to be replenished. The difference in the character of the melt geometry
408 between our two transects suggests that melt is dynamic, and we have imaged two different
409 stages in the melt migration process.

410 Our observation of broadly distributed melt, far from the ridge axis requires another
411 dynamic component to create upwelling, such as small-scale convection due to lithospheric
412 instabilities (Richter, 1973). In these models, the earliest drips start beneath 5-30 Myr seafloor
413 for cases with a low viscosity asthenosphere ($\sim 10^{17}$ - 10^{18} Pa s) (Buck and Parmentier, 1986), in
414 agreement with our observation. Alternatively, upwellings could be driven by mantle chemical
415 heterogeneity. Broadly distributed melt will also lower mantle viscosity and further enhance
416 asthenospheric convection. This could also explain why seafloor subsidence and heat flow are
417 more muted than predicted beneath the oldest seafloor, > 70 Myr (Parsons and Sclater, 1977).

418 Our observations of melt in a variety of forms unify seemingly discrepant observations of
419 melt channels at the base of the plates (Mehouachi and Singh, 2018; Naif et al., 2013; Stern et

420 al., 2015), including the lack thereof (Key et al., 2013), and broadly distributed melt in the
421 asthenosphere (Forsyth et al., 1998). It suggests melt is persistent over geologic timescales, yet
422 dynamic in character. Since melt would decrease the viscosity of the mantle, it would also define
423 the plate. Therefore, plate thickness and character, and lithosphere-asthenosphere coupling are
424 highly dynamic, and dependent on melt dynamics. Episodic melt-enhanced buoyancy beneath
425 the ridge could increase the influence of ridge-push in driving plate motions. In addition, melt
426 channels at the base of the lithosphere would reduce its basal drag resistance. Enhanced melt
427 buoyancy and also enhanced decoupling may be key to explaining divergent plate motions
428 beneath the Atlantic in the absence of significant drivers from surrounding subducting slabs.
429 Plate spreading may be further assisted by deep upwellings from the lower mantle beneath the
430 Atlantic that have been proposed based on a thinned mantle transition zone (Agius et al., 2021).
431 In addition, interplay between upwelling and channelizing could result in temporal variations in
432 forcing, and explain observed plate velocity variability (Coli et al., 2014). Melt dynamics could
433 play a larger role in controlling plate motions than previously thought. Understanding the role of
434 melt generation and migration as a driving force will be needed for a complete understanding of
435 plate tectonics.

436 5. CONCLUSIONS

437 We image the oceanic lithosphere and asthenosphere in the region near the equatorial
438 Mid-Atlantic Ridge using S_p receiver functions. The LAB increases monotonically with age
439 from 30 to 80 ± 5 km depth in one location, but the LAB is sporadically detected at $20 - 80 \pm$ km
440 depth in other regions. The locations of the LAB detections and depths are consistent with
441 anomaly structures in the resistivity and surface wave-derived shear velocity models when the
442 resolutions of the approaches are considered. The sharp LAB discontinuities (6 – 15 % over < 30

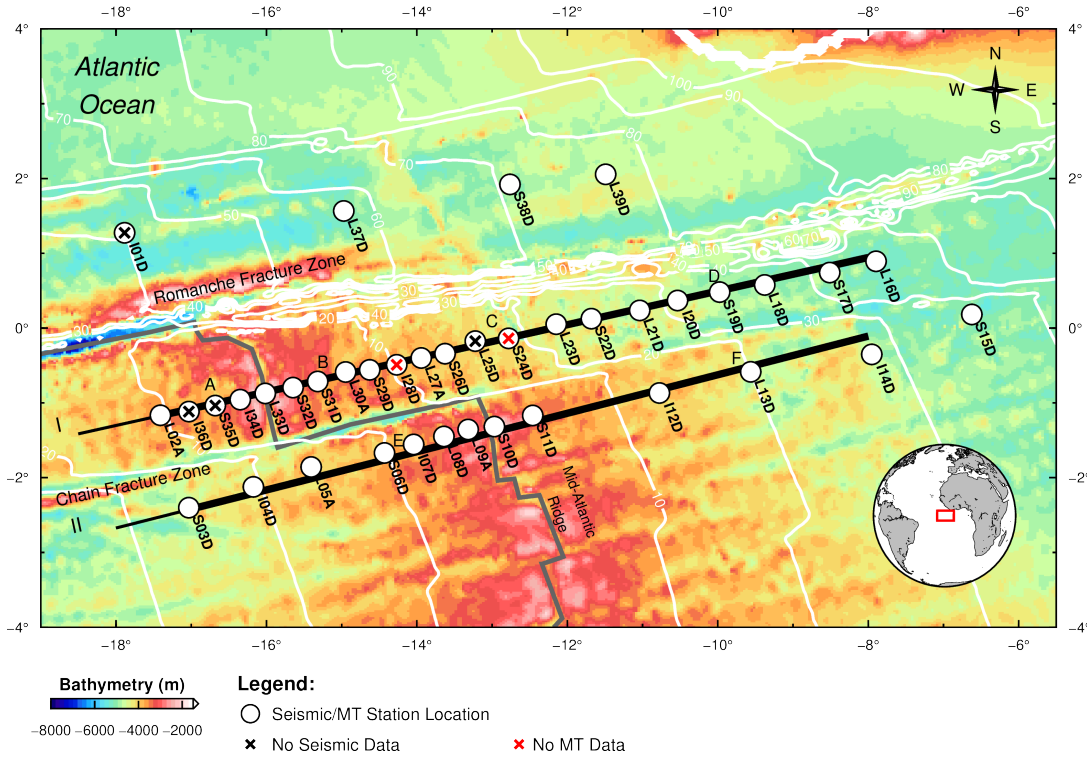
443 km depth), strong seismic ($V_s < 4.2$ km/s) and MT anomalies ($< 1 \Omega$ m), punctuated anomaly
444 characters, and channel structures are not consistent with a purely thermal model. To explain the
445 LAB discontinuities, seismic, and resistivity anomalies in the asthenosphere requires 1 – 5.5 %
446 partial melt localized in upwellings and also ponded beneath the lithosphere. Small scale
447 convection may explain off-axis melt supply. The observations of melt with variable character
448 reconciles previous seemingly discrepant reports from different studies and suggests we have
449 imaged two different stages of melt migration. Melt episodically rises from depth, ponds beneath
450 the plate, and accumulates before eventually leaving the system. Since the presence of melt
451 would define the plate, it suggests that the LAB is dynamic, varying according to mantle
452 dynamics and melt generation and migration. Also, melt dynamics likely play a larger role in
453 driving plate motions than previously thought, with melt buoyancy aiding ridge push and
454 reduced viscosity enabling plate motions.

455

456 **ACKNOWLEDGMENTS**

457 We thank the captain and crew of the R/V Marcus Langseth and the RRS Discovery and also the
458 scientific technicians. We thank K. Davis for assistance with the schematic in Fig. 8. C.A.R. and
459 N.H. were funded by the Natural Environment Research Council (NE/M003507/1) (PI-LAB) and
460 the European Research Council (GA 638665) (EURO-LAB). J.M.K. was funded by the Natural
461 Environment Research Council (NE/M004643/1). S.C. was funded by the National Science
462 Foundation under grant OCE-1536400 (CA-LAB). D.S. was supported by the Portuguese
463 Science and Technology Foundation (FCT/Fundação para a Ciência e Tecnologia), under project
464 PTDC/CTA-GEF/30264/2017 and UIDB/50019/2020 – IDL

465



467

468 **Figure 1**469 **Map of study region.** Background color shows bathymetry. Inset map shows global location.

470 Large white circles show seismic and MT station locations. X's indicate locations where no data

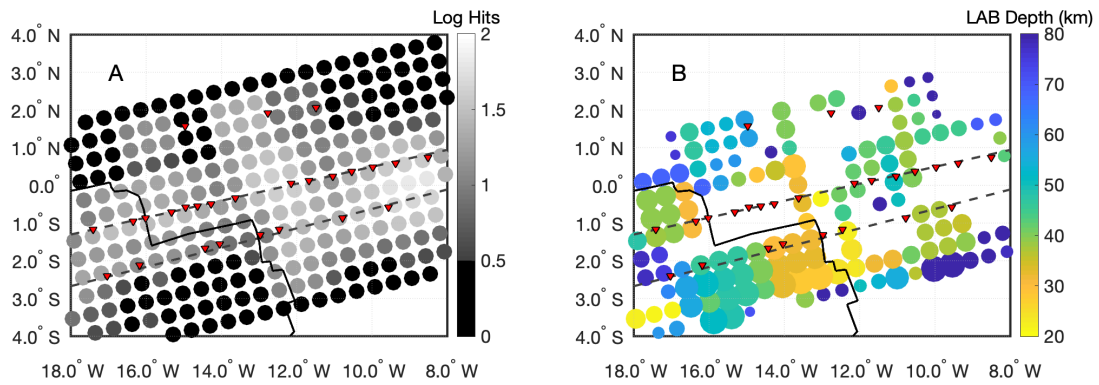
471 was used in the seismic (black) and MT (red) analysis. Dark grey line shows the plate boundary.

472 White lines show age contours (in Myr) (Muller et al., 2008). Thick black lines indicate transect

473 locations, I (northern) and II (southern), with slightly longer limits (thin black line) used in the

474 shear-wave velocity and receiver function transects shown in Fig. 4. Anomaly locations are

475 indicated by the capital letters.



476

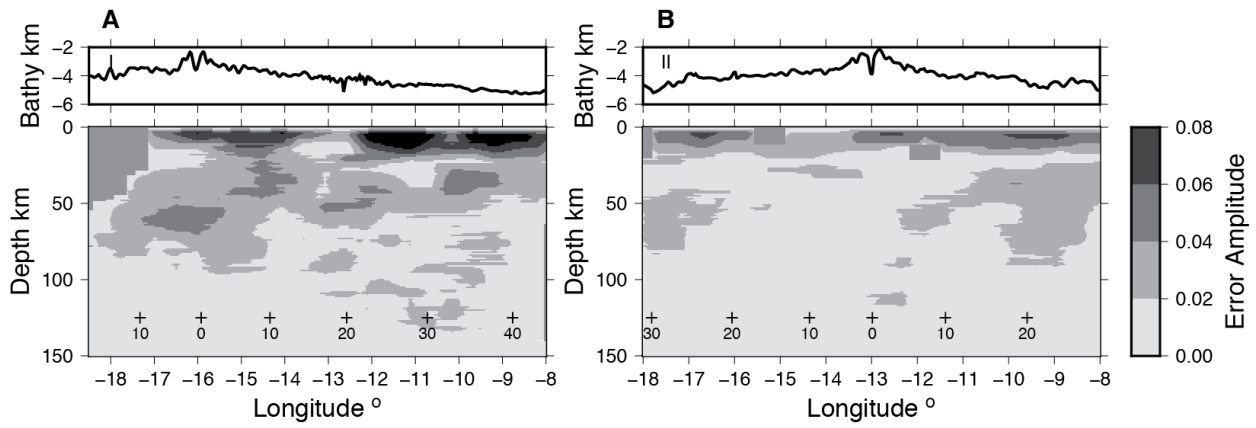
477

478 **Figure 2**

479 **Sp receiver function hit count map and map view of bins with a LAB phase.** A) hit count
 480 map at 60 km depth. Grey shading indicates the number of waveforms averaged into the bin in
 481 $\text{Log}_{10}(\text{Hits})$. B) Circles indicate the bin location and color indicates the depth to the LAB. Circle
 482 size corresponds to the inverse of error, and bins where the error exceeds the amplitude of the
 483 data are not plotted. Black line shows the plate boundary, and dark grey dashed lines show the
 484 locations of the two transects. Inverted red triangles show the stations used in this study.

485

486



487

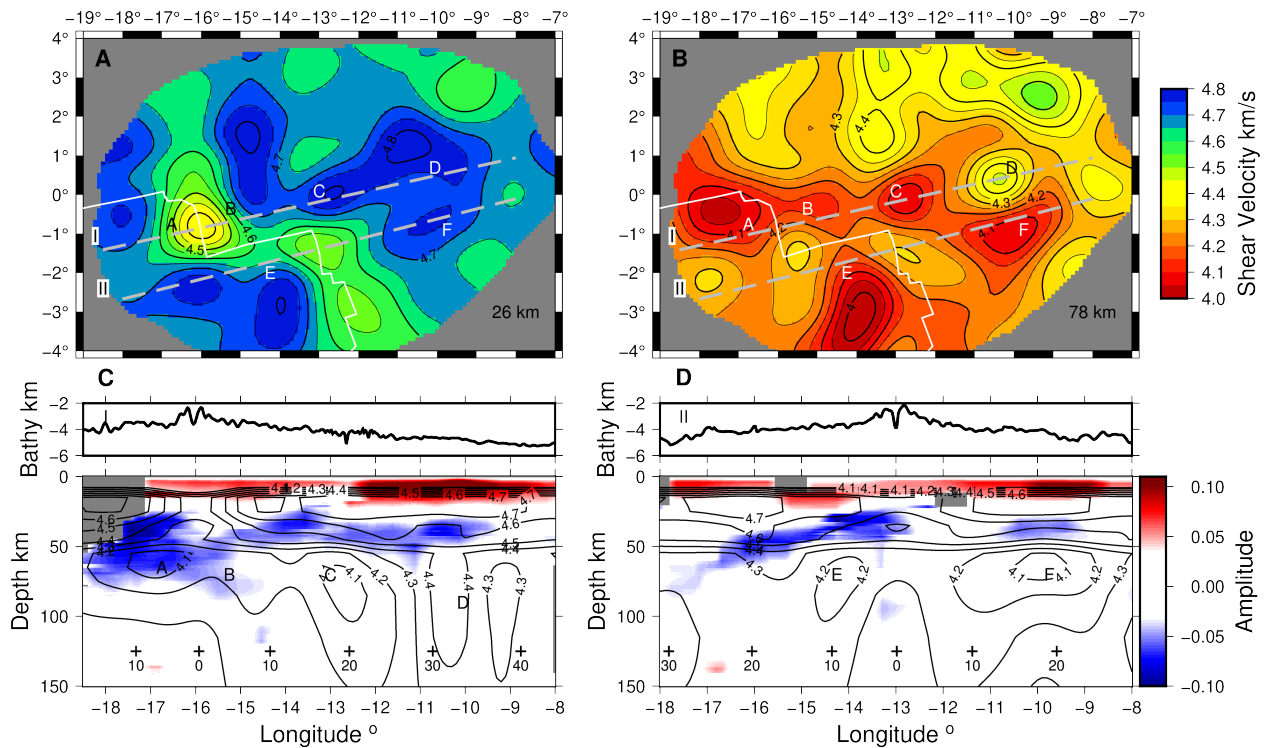
488 **Figure 3**

489 **Sp receiver function amplitude error.** Here we present 95 % confidence limits on the
490 amplitude of the data stack in transect I the north (A) and transect II in the south (B) as shown in
491 Figure 1.

492

493

494



495

496 **Figure 4**

497 **Shear-wave velocity model inferred from inversion of surface waves and Sp receiver**

498 **functions.** Shear-wave velocities from surface waves are shown in map view by colors and

499 contours (red for slow and blue for fast) at A) 26 km depth to illustrate variability owing to plate

500 thickening and B) 78 km depth to illustrate the structure of the punctuated anomalies. White line

501 shows the plate boundary. Dashed grey lines indicate transect locations. Transects through the

502 receiver function and shear-wave models are shown C) and D) for transects I and II. Sp

503 converted phases that result from velocity increases with depth are shown in red and those from

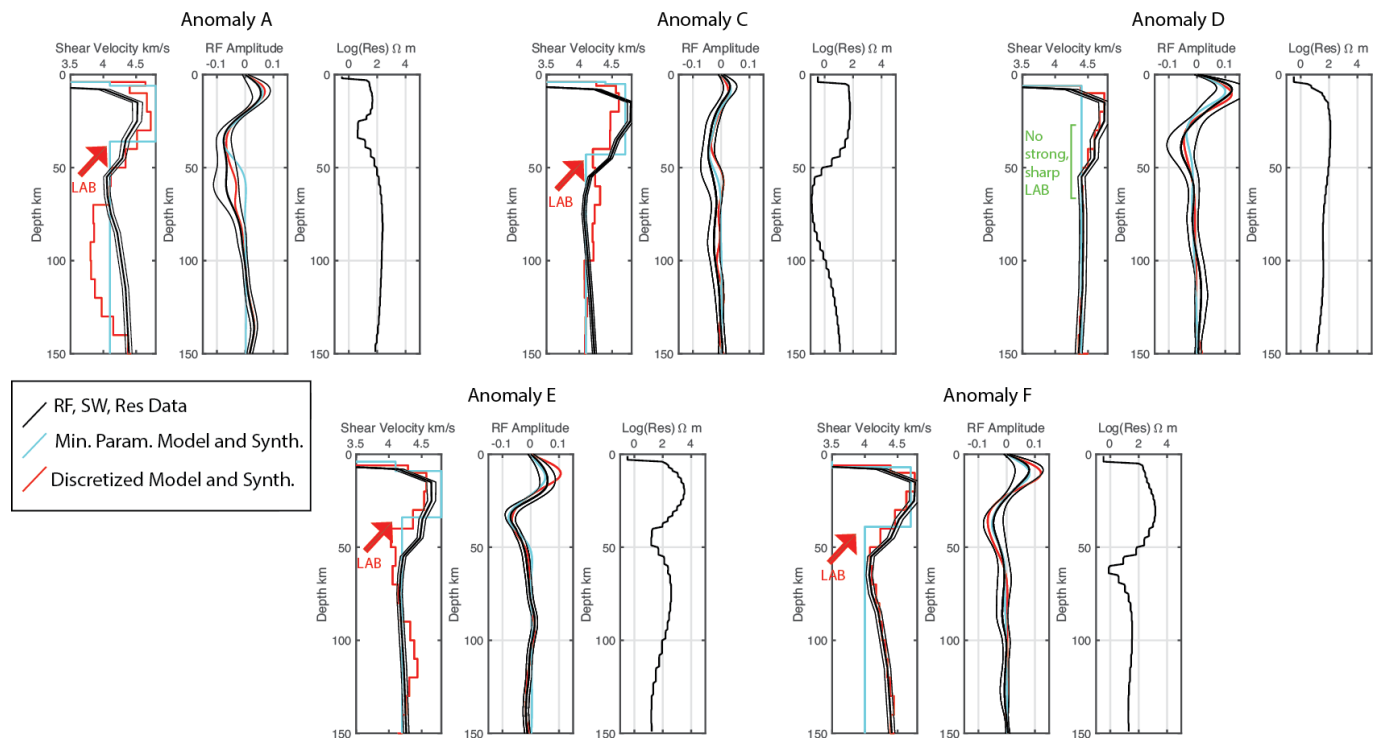
504 decreases with depth are shown in blue. Seafloor bathymetry is plotted above the transects. Grey

505 areas show regions with < 3 hits per bin. Shear-wave velocity from surface waves is shown as

506 black contours with contour labels in km/s. Black crosses show seafloor ages (in Myr) as labeled.

507 Depths are with respect to the sea surface. Anomaly locations are labelled by capital letters.

508



509

510

511 **Figure 5**

512 **1-D Comparisons of main anomalies.** MT imaging (right panels) is compared to the receiver

513 function (RF) data (middle panel, thick black) and 95 % confidence limits (middle panel, thin

514 black) and the shear-wave velocities inferred from surface waves (left panel, thick black) and

515 corresponding 95 % confidence limits (left panel, thin black). Synthetic receiver functions and

516 corresponding shear velocity models from 2 different modelling approaches: a minimum

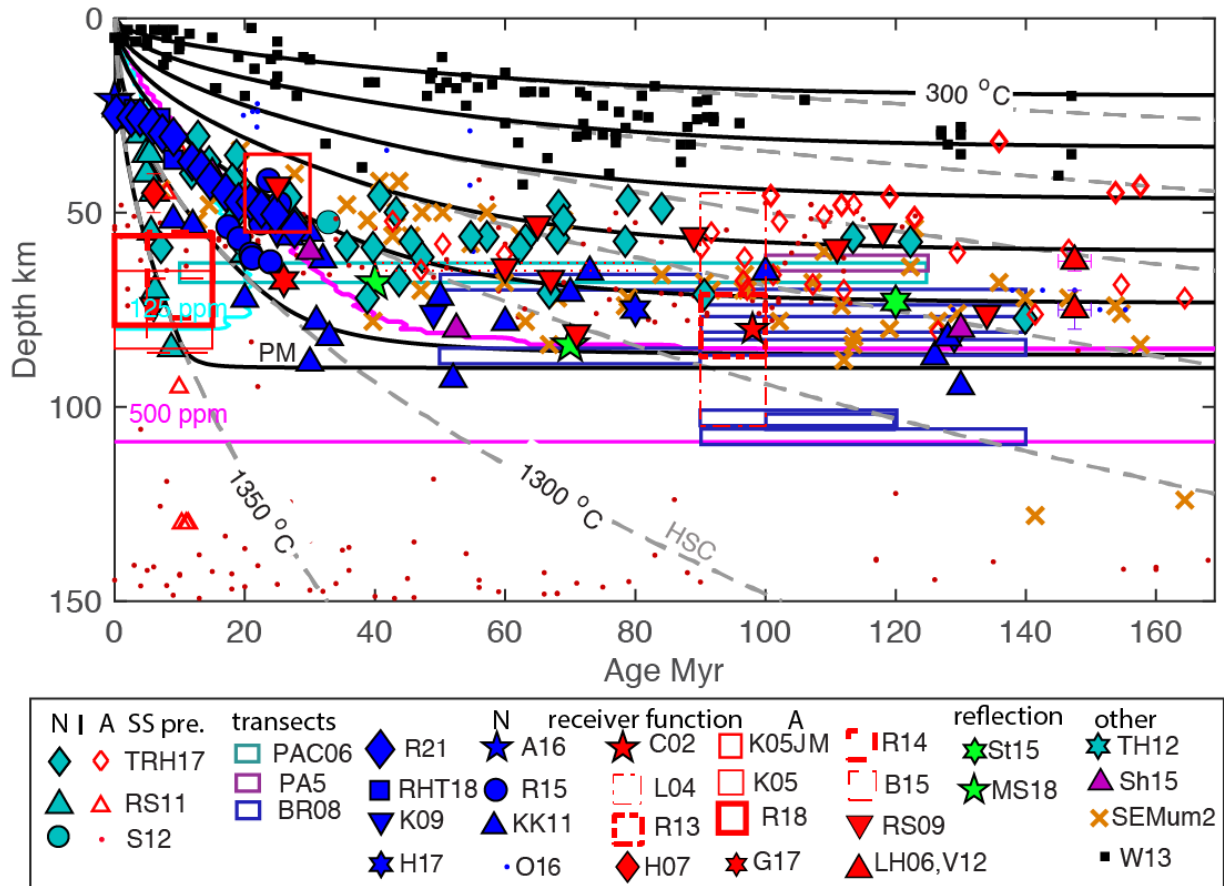
517 parameterisation (blue) and an over parameterisation (red) are shown in the middle and left

518 panels, respectively. Receiver functions are only sensitive to changes in velocity, although we

519 show possible absolute velocities for comparison with the shear-wave velocities from surface

520 waves. The five major interpreted anomalies as labelled in Fig. 7. Red arrows highlight seismic

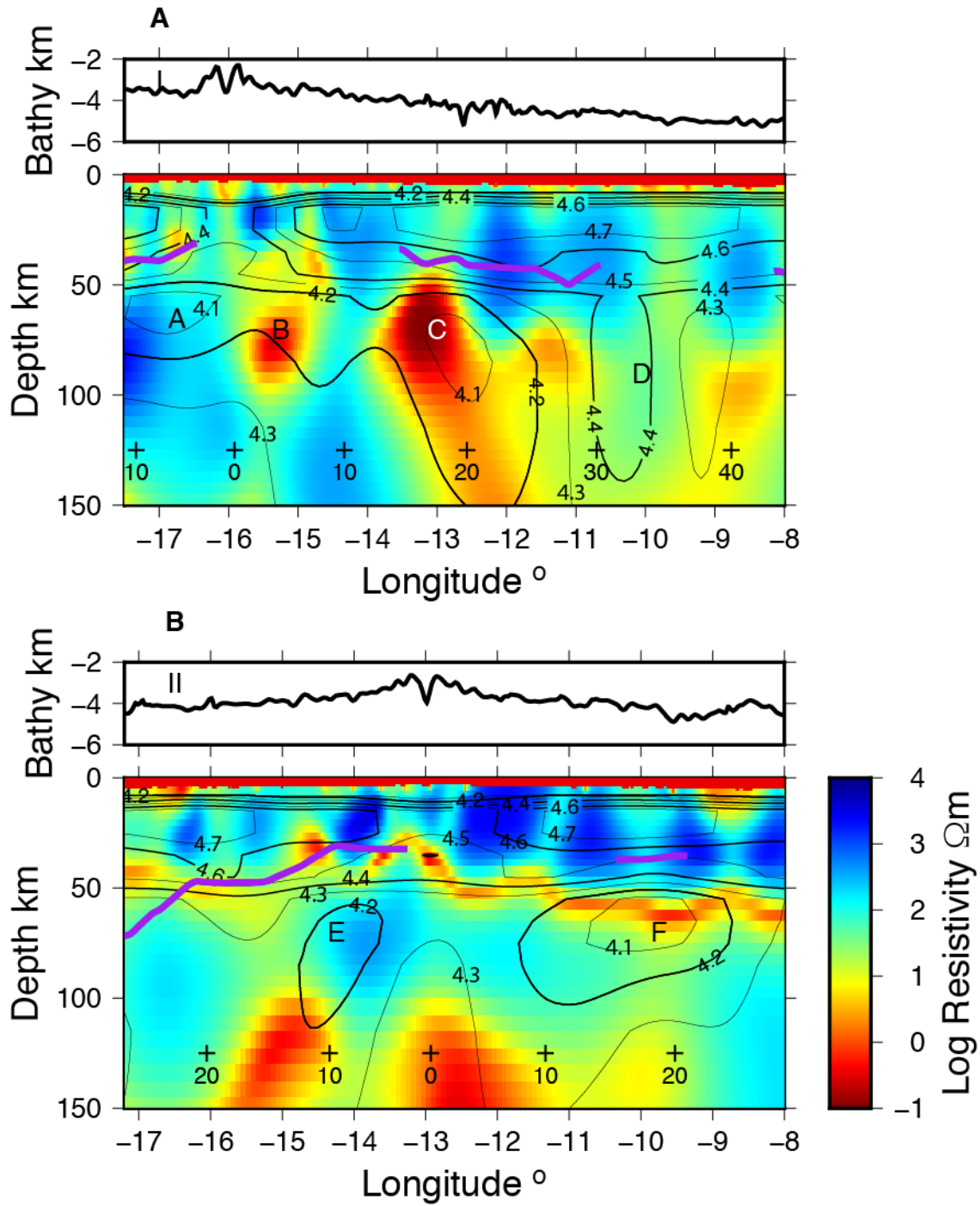
521 low velocity zones, significant LAB phases from receiver functions and the depth of the strong
 522 sharp drop in velocity in the minimum parameterization model. Green lines show the location
 523 where no LAB phase is significant and no slow shear-wave velocity anomaly exists in the shear-
 524 wave tomography from surface waves, i.e., the interpreted lithospheric drip.
 525



526
 527
 528 **Figure 6**
 529 **Discontinuity depths from the western side of transect II in the south compared to other**
 530 **observations.** Thermal contours are plotted for the half-space cooling model (HSC; grey dashed
 531 lines) and the plate model assuming a 90 km thick plate (PM; black lines) at 200 °C interval and
 532 also a contour very close to the potential temperature, 1350 °C. The solidi for a mildly hydrated

533 mantle are shown for 125 ppm (cyan) and 500 ppm (pink) water assuming a plate model and 90
534 km plate thickness. Depths are plotted relative to the seafloor with submarine results corrected
535 from the depth beneath sea surface by the amount listed, if any. SS precursor results from the
536 entire Pacific including (TRH17, RS11, and S12) are sorted into normal lithosphere (N; cyan)
537 and anomalous (A; red) lithosphere affected by hotspots. Transect studies that encompass a range
538 of ages are shown as boxes with fixed thickness (5 km), including: PAC06; PA5 -5, km; and
539 BR08, -4 km. Active source studies (solid green symbols) include MS18, -4 km and St15.
540 Receiver function results from normal (N) ocean lithosphere unaffected by hotspots (solid blue
541 symbols) include this study (R21, -4 km), Cascadia (RHT18, -3 km), offshore California (R15, -
542 3 km), western Pacific (O16), Circum-Pacific (KK11), off-shore Japan (K09), Gloria Fault in the
543 Atlantic (H17); and the Juan de Fuca Ridge (A16). Receiver function studies from ocean island
544 hotspot studies (A, anomalous) are shown as solid red symbols or red boxes where the studies
545 encompass a range of ages or depths, with -5 km depth correction applied to island studies
546 (LH06, V12, K05JM, L04, H07, G17, R14, B15, K05) and the listed amount applied to
547 submarine studies: R13, -4 km and C02. The depths of the minimum velocity in the low-velocity
548 zone beneath the Pacific from surface wave model SEMum2 (-4 km) are shown as orange x's.
549 Oceanic effective elastic thickness estimates are shown by black squares. Depths from a sS
550 precursor result (TH12) is shown by a cyan star and a P_0/S_0 result (Sh15) is shown by purple
551 triangles. For a complete set of references please refer to Rychert et al., (2020).

552

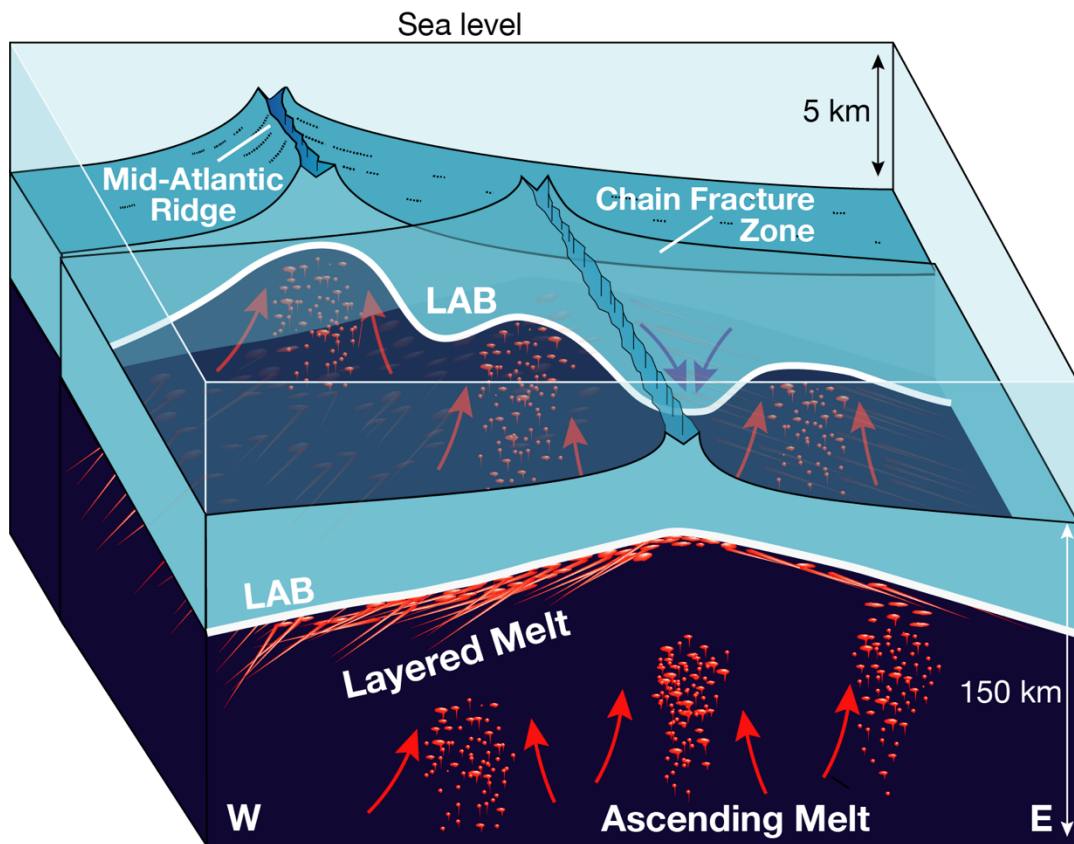


553

554 **Figure 7**

555 **Summary of scientific results.** Results from all three methods are presented along the transects
 556 (thick black lines, Fig. 1). Background color shows resistivity. Black contours show the shear-
 557 wave seismic velocity model from surface waves. Thick purple line shows negative polarity

558 phase from the Sp receiver functions with amplitudes that exceed 95 % confidence limits.
559 Seafloor bathymetry is plotted above the transects. Black crosses show seafloor ages (in Myr) as
560 labeled. Letters indicate anomalies discussed in the text. Depths are with respect to the sea
561 surface.



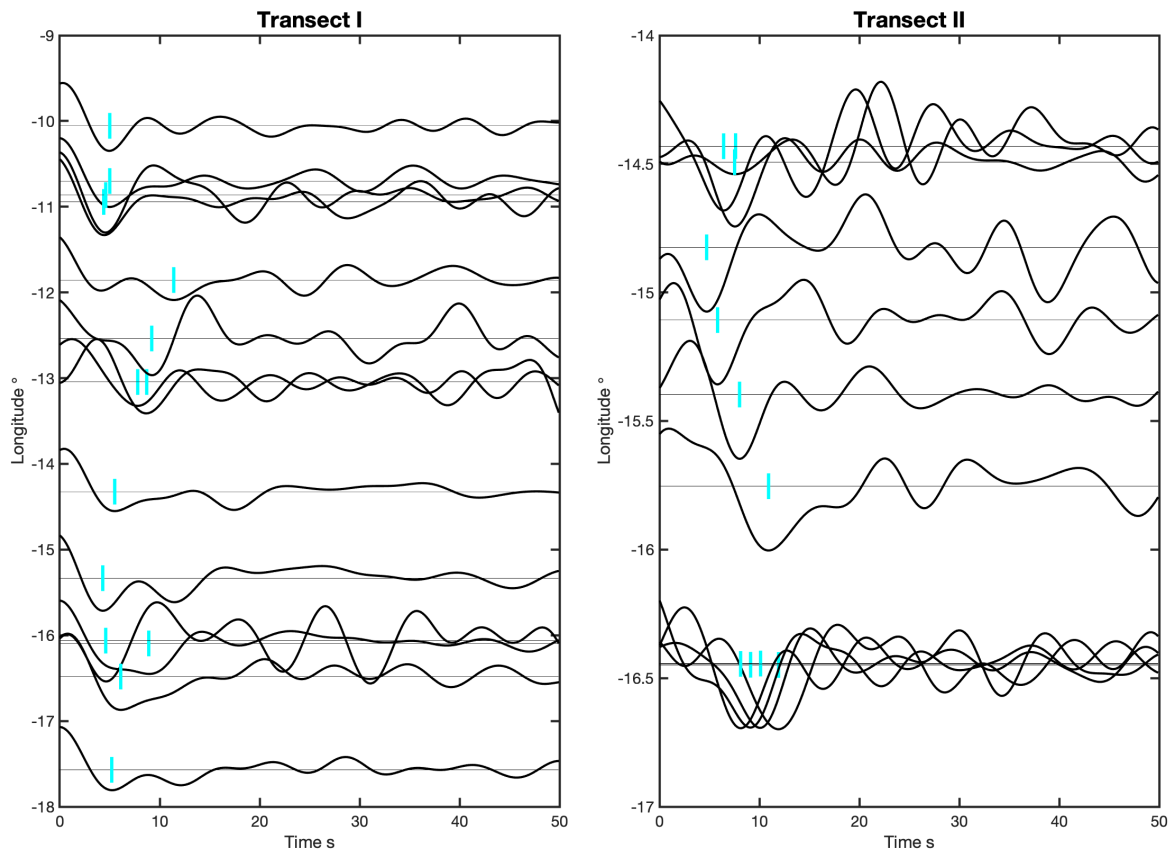
562
563 **Figure 8**
564 **Schematic summary of the interpretation of the results.** Front panel shows transect II where
565 melt layers define the base of the plate, with gradually decreasing amounts of melt with depth in
566 the west and a thin melt channel in the east. Partial melt from either chemical heterogeneity
567 and/or small-scale convection ascends from depth. Back panel shows transect I where the age

568 progression of the plate is more complex, possibly owing to alteration by small-scale convection.

569 The LAB is shown as the thick white line.

570

571

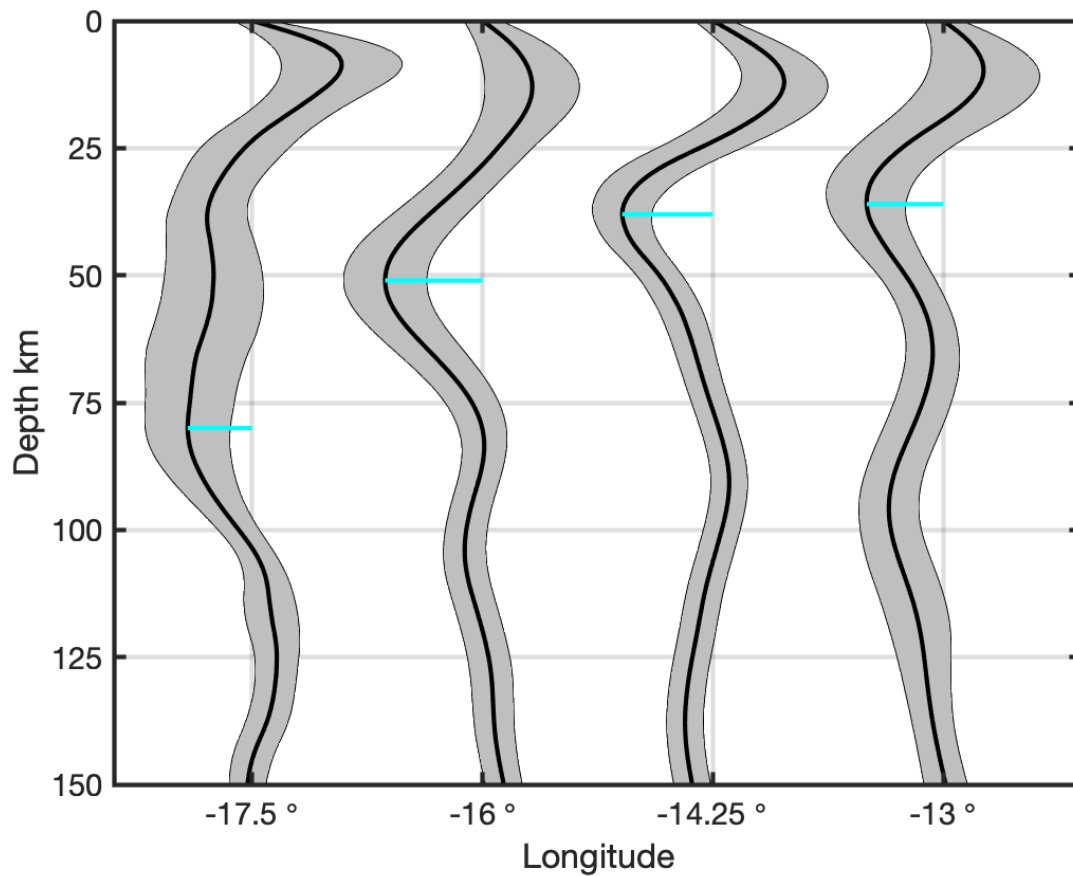


572

573 **Figure S1**

574 **Individual S-to-P receiver function examples.** Receiver functions examples with signal to
575 noise ratios > 10 in the raw data that are stacked and highly weighted in the bins located beneath
576 transects I (left) and II (right) are shown. The x-axes correspond to the differential time before
577 the S-wave. The y-axes correspond to the longitude of the conversion point. These receiver
578 functions are converted at any depth beneath the transect. In the final model these examples are

579 also stacked with many more seismograms of similar quality. Therefore, a 1-to-1 correlation with
580 the models presented in Figure 1 and 4 is not expected. A positive phase is imaged at < 5 s that is
581 related to the Moho. It is shallower in some cases owing to interference with internal Moho
582 discontinuities. In addition, a negative discontinuity is imaged in transect II (marked by cyan
583 lines) with increasing differential time towards the west, corresponding to the interpreted
584 thickening plate. In transect I greater complexity is imaged, and in some cases two negative
585 discontinuities exist, potentially related to complex topography. Overall, the figure demonstrates
586 what goes into the stacks. Other phases are present besides the Moho-related phase and the LAB
587 in some receiver functions. Additional phases besides the Moho-related phase and the LAB are
588 likely related to noise because they stack out in the final model. The figure demonstrates that the
589 Moho and/or Moho-related phase and LAB phases exist in the raw receiver functions and do not
590 correspond to wrongly interpreted noise. Phases that are not significantly different from zero
591 according to formal error are not plotted or interpreted in Fig. 7.



592

593

594 **Figure S2**

595 **Vertical receiver functions from the stacked model from the western half of transect II in**

596 **the south.** Thick black lines show the receiver functions and grey region show the 95 %

597 confidence limits. Cyan lines show the depths of the interpreted LAB phases.

598 **REFERENCES CITED**

599 Agius, M., Rychert, C.A., Harmon, N., Kendall, J.M., Tharimena, S., 2021. Transition zone
600 thinning beneath the Mid-Atlantic Ridge suggests whole mantle convection. *Nature* 589,
601 doi:10.1038/s41586-020-03139-x.

602 Agius, M.R., Harmon, N., Rychert, C.A., Tharimena, S., Kendall, J.M., 2018. Sediment
603 characterization at the equatorial Mid-Atlantic Ridge from P-to-S teleseismic phase conversions
604 recorded on the PI-LAB Experiment. *Geophysical Research Letters* 45,
605 doi:10.1029/2018gl080565.

606 Baba, K., Chave, A.D., Evans, R.L., Hirth, G., Mackie, R.L., 2006. Mantle dynamics beneath the
607 East Pacific Rise at 17 degrees S: Insights from the Mantle Electromagnetic and Tomography
608 (MELT) experiment. *J. Geophys. Res.* 111, doi:10.1029/2004JB003598.

609 Beghein, C., Yuan, K.Q., Schmerr, N., Xing, Z., 2014. Changes in seismic anisotropy shed light
610 on the nature of the Gutenberg Discontinuity. *Science* 343, doi:10.1126/science.1246724.

611 Bell, S., Ruan, Y.Y., Forsyth, D.W., 2016. Ridge asymmetry and deep aqueous alteration at the
612 trench observed from Rayleigh wave tomography of the Juan de Fuca plate. *J. Geophys. Res.*
613 121, doi:10.1002/2016JB012990.

614 Buck, W.R., Parmentier, E.M., 1986. Convection beneath young oceanic lithosphere -
615 Implications for thermal structure and gravity. *J. Geophys. Res.* 91,
616 doi:10.1029/JB091iB02p01961.

617 Burgos, G., Montagner, J.P., Beucler, E., Capdeville, Y., Mocquet, A., Drilleau, M., 2014.
618 Oceanic lithosphere-asthenosphere boundary from surface wave dispersion data. *J Geophys Res-*
619 *Sol Ea* 119, doi:10.1002/2013jb010528.

620 Cline, C.J., Faul, U.H., David, E.C., Berry, A.J., Jackson, I., 2018. Redox-influenced seismic
621 properties of uppermantle olivine. *Nature* 555, doi:10.1038/nature25764.

622 Coli, L., Stotz, I., Bunge, H.P., Smethurst, M., Clark, S., Iaffaldano, G., Tassara, A.,
623 Guillocheau, F., Bianchi, M.C., 2014. Rapid South Atlantic spreading changes and coeval
624 vertical motion in surrounding continents: Evidence for temporal changes of pressure-driven
625 upper mantle flow. *Tectonics* 32, doi:10.1002/2014TC003612.

626 Conder, J.A., Forsyth, D.W., Parmentier, E.M., 2002. Asthenospheric flow and asymmetry of the
627 East Pacific Rise, MELT area. *J. Geophys. Res.* 107, doi:10.1029/2001JB000807.

628 Dziewonski, A.M., Anderson, D.L., 1981. Preliminary reference Earth model. *Phys. Earth*
629 *Planet. Inter.* 25

630 Fischer, K., Rychert, C., Dalton, C., Miller, M., Beghein, C., Schutt, D., 2020. A comparison of
631 oceanic and continental mantle lithosphere. *Phys Earth Planet In* 309,
632 doi:10.1016/j.pepi.2020.106600.

633 Forsyth, D.W., Scheirer, D.S., Webb, S.C., Dorman, L.M., Orcutt, J.A., Harding, A.J.,
634 Blackman, D.K., Morgan, J.P., Detrick, R.S., Shen, Y., Wolfe, C.J., Canales, J.P., Toomey, D.R.,
635 Sheehan, A.F., Solomon, S.C., Wilcock, W.S.D., Team, M.S., 1998. Imaging the deep seismic
636 structure beneath a mid-ocean ridge: The MELT experiment. *Science* 280,
637 doi:10.1126/science.280.5367.1215.

638 French, S.W., Lekic, V., Romanowicz, B., 2013. Waveform Tomography Reveals Channeled
639 Flow at the Base of the Oceanic Asthenosphere. *Science* 342, doi:10.1126/science.1241514.

640 Gaherty, J.B., Jordan, T.H., Gee, L.S., 1996. Seismic structure of the upper mantle in a central
641 Pacific corridor. *J. Geophys. Res.* 101, doi:10.1029/96JB01882.

642 Harmon, N., Forsyth, D.W., Weeraratne, D.S., 2009. Thickening of young Pacific lithosphere
643 from high-resolution Rayleigh wave tomography: A test of the conductive cooling model. *Earth*
644 *Planet. Sci. Lett.* 278, doi:10.1016/J.Epsl.2008.11.025.

645 Harmon, N., Forsyth, D.W., Weeraratne, D.S., Yang, Y.J., Webb, S.C., 2011. Mantle
646 heterogeneity and off axis volcanism on young Pacific lithosphere. *Earth Planet. Sci. Lett.* 311,
647 doi:10.1016/J.Epsl.2011.09.038.

648 Harmon, N., Rychert, C., Kendall, J., Tharimena, S., Bogiatzis, P., Agius, M., 2020. Evolution of
649 the oceanic lithosphere in the equatorial Atlantic from Rayleigh Wave tomography, evidence for
650 small-scale convection from the PI-LAB experiment. *Geochem Geophys Geosy Geochem*
651 *Geophys Geosy*, doi:10.1029/2020GC009174.

652 Harmon, N., Rychert, C.A., Agius, M.R., Tharimena, S., Le Bas, T.P., Kendall, J.M., Constable,
653 S., 2018. Marine geophysical investigation of the Chain Fracture Zone in the equatorial Atlantic
654 from the PI-LAB Experiment. *J. Geophys. Res.* 123, doi:10.1029/2018jb015982.

655 Helffrich, G., 2006. Extended-time multitaper frequency domain cross-correlation receiver-
656 function estimation. *B Seismol Soc Am* 96, doi:10.1785/0120050098.

657 Hirth, G., Kohlstedt, D.L., 1995. Experimental constraints on the dynamics of the partially
658 molten upper-mantle .2. Deformation in the dislocation creep regime. *J. Geophys. Res.* 100,
659 doi:10.1029/94JB02128.

660 Jackson, I., Faul, U.H., 2010. Grainsize-sensitive viscoelastic relaxation in olivine: Towards a
661 robust laboratory-based model for seismological application. *Phys. Earth Plan. Int.* 183,
662 doi:10.1016/J.pepi.2010.09.005.

663 Jackson, I., Faul, U.H., Fitz Gerald, J.D., Morris, S.J.S., 2006. Contrasting viscoelastic behavior
664 of melt-free and melt-bearing olivine: Implications for the nature of grain-boundary sliding.
665 *Materials Science and Engineering a-Structural Materials Properties Microstructure and*
666 *Processing* 442, doi:10.1016/J.msea.2006.01.136.

667 Johansen, S.E., Panzner, M., Mittet, R., Amundsen, H.E.F., Lim, A., Vik, E., Landrø, M.,
668 Arntsen, B., 2019. Deep electrical imaging of the ultraslow-spreading Mohns Ridge. *Nature* 567,
669 doi:10.1038/s41586-019-1010-0.

670 Karato, S.I., Olugboji, T., Park, J., 2015. Mechanisms and geologic significance of the mid-
671 lithosphere discontinuity in the continents. *Nature Geoscience* 8, doi:10.1038/Ngeo2462.

672 Katz, R., 2010. Porosity-driven convection and asymmetry beneath mid-ocean ridges. *Geochem.*
673 *Geophys. Geosyst.* 11

674 Kawakatsu, H., Kumar, P., Takei, Y., Shinohara, M., Kanazawa, T., Araki, E., Suyehiro, K.,
675 2009. Seismic evidence for sharp lithosphere-asthenosphere boundaries of oceanic plates.
676 *Science* 324, doi:10.1126/science.1169499.

677 Key, K., Constable, S., Liu, L., Pommier, A., 2013. Electrical image of passive mantle upwelling
678 beneath the northern East Pacific Rise. *Nature* 495, doi:10.1038/nature11932.

679 Lekic, V., Fischer, K.M., 2017. Interpreting spatially stacked Sp receiver functions. *Geophys. J.*
680 *Int.* 210, doi:10.1093/gji/ggx206.

681 Mehouchi, F., Singh, S., 2018. Water-rich sublithospheric melt channel in the equatorial
682 Atlantic Ocean. *Nat. Geosci.* 11, doi:10.1038/s41561-017-0034-z.

683 Morgan, J.P., Parmentier, E.M., Lin, J., 1987. Mechanisms for the origin of midocean ridge axial
684 topography - Implications for the thermal and mechanical structure of accreting plate boundaries.
685 *J. Geophys. Res.* 92, doi:10.1029/JB092iB12p12823.

686 Muller, R.D., Sdrolias, M., Gaina, C., Roest, W.R., 2008. Age, spreading rates, and spreading
687 asymmetry of the world's ocean crust. *Geochem. Geophys. Geosyst.* 9,
688 doi:10.1029/2007gc001743.

689 Naif, S., Key, K., Constable, S., Evans, R.L., 2013. Melt-rich channel observed at the
690 lithosphere-asthenosphere boundary. *Nature* 495, doi:10.1038/nature11939.

691 Parker, R.L., Whaler, K.A., 1981. Numerical methods for establishing solutions to the inverse
692 problem of electromagnetic induction. . *J. Geophys. Res.* 86, doi:10.1029/JB086iB10p09574.

693 Parmentier, E.M., Morgan, J.P., 1990. Spreading Rate Dependence of 3-Dimensional Structure
694 in Oceanic Spreading Centers. *Nature* 348, doi:10.1038/348325a0.

695 Parsons, B., Sclater, J.G., 1977. Analysis of Variation of Ocean-Floor Bathymetry and Heat-
696 Flow with Age. *J. Geophys. Res.* 82, doi:10.1029/JB082i005p00803.

697 Richter, F.M., 1973. Convection and large-scale circulation of mantle. *J. Geophys. Res.* 78,
698 doi:10.1029/JB078i035p08735.

699 Rychert, C.A., Hammond, J.O.S., Harmon, N., Kendall, J.M., Keir, D., Ebinger, C., Bastow,
700 I.D., Ayele, A., Belachew, M., Stuart, G., 2012. Volcanism in the Afar Rift sustained by
701 decompression melting with minimal plume influence. *Nat Geosci* 5, doi:10.1038/Ngeo1455.

702 Rychert, C.A., Harmon, N., 2018. Predictions and observations for the oceanic lithosphere from
703 S-to-P receiver functions and SS precursors. *Geophys. Res. Lett.* 45, doi:10.1029/2018gl077675.

704 Rychert, C.A., Harmon, N., Constable, S., Wang, S., 2020. The Nature of the Lithosphere-
705 Asthenosphere Boundary. *J. Geophys. Res.*, doi:10.1029/2018JB016463.

706 Rychert, C.A., Harmon, N., Tharimena, S., 2018a. Scattered wave imaging of the oceanic plate
707 in Cascadia. *Sci Adv* 4, doi:10.1126/sciadv.aao1908.

708 Rychert, C.A., Harmon, N., Tharimena, S., 2018b. Seismic Imaging of the Base of the Ocean
709 Plates, in: Yuan, H. (Ed.), *Lithospheric Discontinuities*. AGU Monographs, Washington DC, pp.
710 71-87, doi:10.1002/9781119249740.ch4.

711 Rychert, C.A., Shearer, P.M., 2009. A Global View of the Lithosphere-Asthenosphere Boundary.
712 *Science* 324, doi:10.1126/science.1169754.

713 Saikia, U., Rychert, C.A., Harmon, N., Kendall, J.M., 2020. Sediment Structure at the Equatorial
714 Mid-Atlantic Ridge Constrained by Seafloor Admittance using data from the PI-LAB
715 experiment. *Marine Geophys. Res.*, doi:10.1029/2018GL080565.

716 Saikia, U., Rychert, C.A., Harmon, N., Kendall, J.M., 2021. Upper mantle anisotropic shear
717 velocity structure at the equatorial Mid-Atlantic Ridge constrained by Rayleigh wave group
718 velocity analysis from the PI-LAB experiment *Geochem Geophys Geosy Geochem Geophys*
719 *Geosy*, doi:10.1029/2020GC009495

720 Shibutani, T., Ueno, T., Hirahara, K., 2008. Improvement in the extended-time multitaper
721 receiver function estimation technique. *B Seismol Soc Am* 98, doi:10.1785/0120070226.

722 Sim, S.J., Spiegelman, M., Stegman, D.R., Wilson, C., 2020. The influence of spreading rate and
723 permeability on melt focusing beneath mid-ocean ridges. *Phys. Earth & Planet. Int.* 304,
724 doi:10.1016/j.pepi.2020.106486.

725 Sparks, D., Parmentier, E., 1991. Melt extraction from the mantle beneath spreading centers.
726 *Earth & Planet. Sci. Lett.* 105, doi:10.1016/0012-821X(91)90178-K.

727 Stern, T.A., Henrys, S.A., Okaya, D., Louie, J.N., Savage, M.K., Lamb, S., Sato, H., Sutherland,
728 R., Iwasaki, T., 2015. A seismic reflection image for the base of a tectonic plate. *Nature* 518,
729 doi:10.1038/nature14146.

730 Tan, Y., Helmberger, D.V., 2007. Trans-Pacific upper mantle shear velocity structure. *J.*
731 *Geophys. Res.* 112, doi:10.1029/2006JB004853.

732 Tharimena, S., Rychert, C., Harmon, N., White, P., 2017. Imaging Pacific lithosphere seismic
733 discontinuities Insights from SS precursor modeling. *J. Geophys. Res.* 122,
734 doi:10.1002/2016jb013526.

735 Thybo, H., 2006. The heterogeneous upper mantle low velocity zone. *Tectonophysics*
736 *Tectonophysics* 416, doi:10.1016/j.tecto.2005.11.021.

737 Toomey, D.R., Wilcock, W.S.D., Conder, J.A., Forsyth, D.W., Blundy, J.D., Parmentier, E.M.,
738 Hammond, W.C., 2002. Asymmetric mantle dynamics in the MELT region of the East Pacific
739 Rise. *Earth Planet. Sci. Lett.* 200, doi:10.1016/S0012-821X(02)00655-6.

740 Wang, S., Constable, S., Rychert, C., Harmon, N., 2020. A lithosphere-asthenosphere boundary
741 and partial melt estimated using marine magnetotelluric data at the central Middle Atlantic
742 Ridge. doi:10.1029/2020GC009177.

743 Yamauchi, H., Takei, Y., 2016. Polycrystal anelasticity at near-solidus temperatures. *J. Geophys.*
744 *Res.* 121, doi:10.1002/2016jb013316.
745